Korean J. Chem. Eng., 37(8), 1379-1386 (2020)
DOI: 10.1007/s11814-020-0587-1

pISSN: 0256-1115
eISSN: 1975-7220

Electrodeposited nickel phosphide supported by copper foam for proton exchange membrane water electrolyzer

Kyurim Yeon‡, Junhyeong Kim‡, Hyunki Kim, Wenwu Guo, Gyeong Ho Han, Seokjin Hong, and Sang Hyun Ahn†

School of Chemical Engineering and Material Science, Chung-Ang University, 84 Heukseokno, Dongjak-gu, Seoul 06974, Korea
(*Received 24 March 2020 • Revised 6 May 2020 • Accepted 20 May 2020*)

Abstract−The development of high-performance and low-cost electrodes is essential for hydrogen production using a proton exchange membrane water electrolyzer (PEMWE). Herein, we report an electrochemical method for the fabrication of a Ni-P based cathode for a PEMWE single cell. A porous copper foam (CF) is fabricated on carbon paper (CP) by two-step electrodeposition to obtain a large number of active sites for Ni-P formation. The high conductivity of the Cu metallic support is expected to reduce the charge transfer resistance. After the Ni-P electrodeposition on CF, an anodic leaching process is conducted for the selective dissolution of the excess Ni metal formed during the electrodeposition, thus enabling the modification of the electronic structure of the catalyst. The electrode optimized in half-cell tests is used as the cathode for a PEMWE single cell. The PEMWE cells exhibit a current density of 0.67 A/cm^2 at 2.0 V_{cell} which is higher than or comparable to the performance previously reported in the literature.

Keywords: Water Electrolysis, Copper Foam Support, Nickel Phosphide Catalyst, Gas Diffusion Electrode, Electrodeposition

INTRODUCTION

Hydrogen is a clean energy source that can potentially replace fossil fuels in the near future [1]. Among the existing hydrogen production methods, water electrolysis is a promising technology that splits water into hydrogen and oxygen using a photo/electrochemical driving force derived from renewable energy sources with zero pollutant emission [2-4]. Membrane electrode assembly (MEA)-based electrolysis enables to increase the purity of the products by separating the two electrodes, and a higher hydrogen production rate can be obtained by using a proton exchange membrane (PEM) [5,6]. However, due to the acidic environment, the potential catalysts for electrolysis are limited to noble metals [7]. In the anode, platinum-group metal (PGM) oxides such as IrO_x and RuO_x have been used for the oxygen evolution reaction (OER) [8], whereas PGMs that exhibit high activity for hydrogen evolution reaction (HER) have been used in the cathode [7], thus inhibiting the commercialization of water electrolysis systems [9]. In addition, conventional MEAs employing a Pt cathode and an IrO_x anode demonstrated severe performance degradation in PEM-based water electrolysis due to the crossover and agglomeration of the catalysts, indicating that catalyst durability is also an important issue for the commercialization of water electrolysis systems [10].

For the cathode, first-row transition metals have been considered to replace the PGMs because these transition metals are thermodynamically stable in the negative operating potential range where the HER occurs [7]. However, their intrinsic HER activities are much lower than those of PGMs due to the stronger energy of hydrogen adsorption (ΔG_H^*) on their surfaces [11]. Thus, several strategies for improving the intrinsic HER activity of transition metal-based catalysts (e.g., metal alloys [12-14], phosphide- [15,16], sulfide- [17,18], boride- [19,20], and nitride- [21,22] compounds) through the modification of the value of ΔG_H^* to approach zero have been investigated based on the controlled changes of the electronic structure of the catalyst surface [23,24]. In particular, Ni-P has been reported to show outstanding HER activity and durability [25-27]. Furthermore, the Ni/P composition ratio can be adjusted to alter the ΔG_H^* value related to the HER performance [26]. In addition to compositional control, HER performance can also be enhanced by the increase in the number of active sites through the control of morphology or introduction of metallic support [15,28]. In previous studies, electrocatalysts loaded on a three-dimensional (3-D) structured substrate such as Ni foam and CF have shown a large electrochemical surface area and excellent HER performance characteristics [29-31]. Additionally, a metallic support with good electronic conductivity enables fast electron transfer to active sites during the HER [32].

Generally, transition metal phosphide (TMP) catalysts have been fabricated using gas-phase phosphidation [28,31]. However, this method requires the use of a time-consuming process, high temperature (~300 °C), and toxic gases such as PH_3 [33]. Liquid-phase synthesis is another typical method for the preparation of the TMP catalysts, but it also requires a time-consuming (on the order of days) fabrication process and the use of a ligand elimination step after the catalyst synthesis [26,34,35]. In addition, the powders pre-

†To whom correspondence should be addressed.
E-mail: shahn@cau.ac.kr
‡These authors contributed equally.

pared by these chemical synthesis methods must be loaded on the gas diffusion layer (GDL) by a coating process [36]. By contrast, catalyst fabrication by electrodeposition can be performed in a short time at room temperature and ambient pressure [12,37], and the morphological and chemical properties of the catalyst can be changed through simple modifications of the parameters such as electrolyte composition and applied potential, current, and time. In addition, the electrodeposited catalyst on GDL can be directly applied as an electrode for PEMWEs without any additional processing [38].

Unfortunately, the preparation of a thermodynamically stable multi-component catalyst using the electrodeposition method is challenging. Typically, when the electrolyte containing Ni and P precursors is used for the electrodeposition of a Ni-P catalyst, metallic Ni is obtained simultaneously with the desired Ni-P catalyst. This excess Ni on the surface is more thermodynamically unstable than the positively charged Ni coupled with P, so that corrosion of metallic Ni occurs during the HER in an acidic environment [39,40]. To solve the corrosion problem, post-treatment can be used to remove the excess Ni selectively through electrochemical leaching at an appropriate potential in an acidic medium [41,42]. In addition, the removal of metallic Ni is expected to change the electrochemical properties due to the modification of the atomic composition at the catalyst surface [42,43].

In this work, Ni-P electrocatalyst for HER was fabricated by electrodeposition and post-treatment. As a first step, porous CF was electrodeposited on CP acting as the metallic support to provide a greater number of active sites and good electrical conductivity. Then, Ni-P was electrodeposited on the CF under controlled deposition parameters, and the anodic leaching process was applied to remove the excess Ni in order to obtain reasonable HER activity and stability. The optimized Ni-P electrocatalyst exhibited the HER overpotential of 126 mV at −10 mA cm^{-2} in an acidic environment. Furthermore, a PEMWE single cell test demonstrated that the optimized Ni-P cathode exhibited reasonable performance. The results presented herein demonstrate an effective method for the fabrication of Ni-P cathodes that may be applicable to other transition metal-based cathodes.

EXPERIMENTAL

1. Electrochemically Fabricated 3-D Structured CF

The 3-D structured CF was fabricated using a two-step electrodeposition method. Prior to the electrodeposition, the porous CP substrate was immersed in 30 wt% HNO_3 at 50 °C for 30 min, and then the pretreated carbon paper was washed using deionized water [44]. The composition of the electrolyte used for CF electrodeposition was as follows: 0.1 M $CuSO_4 \cdot 5H_2O$ (99.0%, Daejung), 1.0 M $(NH_4)_2SO_4$ (99.0%, Alfa Aesar), and 1.0 M H_2SO_4 (95.0%, Junsei) [45]. The electrolyte was purged with N_2 gas for 30 min to eliminate the dissolved oxygen. A three-electrode cell system, used for CF electrodeposition, was composed of pretreated CP (exposed area: 1.13 cm^2) as the working electrode, a Pt mesh as the counter electrode, and a saturated calomel electrode (SCE) as the reference electrode. For the CF electrodeposition process, a two-step bubble-templating strategy was used. The first step provided the nucleation of Cu seeds on the pretreated carbon paper surface at −13.3 mA/cm^2 for 60 s, and the second step enabled the formation of 3-D networked Cu with vigorous hydrogen generation at −885.0 mA/cm^2 for 40 s.

2. Ni-P Electrodeposition on CF/CP

Ni-P was also fabricated by electrodeposition carried out using a three-electrode cell system. The prepared CF/CP was used as the working electrode (exposed area: 1.13 cm^2), and a Pt wire and SCE were used as the counter and reference electrodes, respectively. The electrolyte for the Ni-P electrodeposition consisted of 0.2 M $NiSO_4 \cdot 6H_2O$ (98.5%, Daejung), 1.0 M $NaH_2PO_2 \cdot H_2O$ (86.0%, Daejung, Korea), and 0.1 M $C_6H_5Na_3O_7$ (99.0%, Daejung). The electrodeposition was performed at $-1.2\ V_{SCE}$ for a constant deposition time of 100 s. N_2 gas was used to purge the electrolyte for 30 min prior to starting the experiment.

3. Anodic Leaching Process for Electrodeposited Ni-P/CF/CP

The as-prepared Ni-P/CF/CP samples were post-treated in a N_2-purged 0.5 M H_2SO_4 solution, and an anodic leaching process was also performed using a three-electrode cell system. NiP/CF/CP (exposed area: 1.13 cm^2) was used as the working electrode, and a carbon rod and SCE were used as the counter and reference electrodes, respectively. Prior to leaching the excess Ni, linear sweep voltammetry (LSV) measurements were performed in the potential range of -0.5~$2.0\ V_{SCE}$ with a scan rate of 10 mV/s to determine the appropriate leaching potential. All measured potentials were converted to reversible hydrogen electrode (RHE) potentials according to $E_{RHE}=E_{SCE}+0.2412+0.0592*pH$.

4. Characterization

For the prepared electrocatalyst samples, surface morphology and bulk crystal structure were investigated by field emission scanning electron microscopy (FESEM, SIGMA, Carl Zeiss) and X-ray diffraction (XRD, New D8-Advance, Bruker), respectively. The atomic composition and electronic structure at the surface of the as-prepared and post-treated nickel phosphide catalysts were characterized using X-ray photoelectron spectroscopy (XPS, K-alpha+, ThermoFisher Scientific). Additionally, bulk atomic compositions were investigated by energy-dispersive spectroscopy (EDS, Thermo NORAN System 7).

5. Electrochemical Measurements

Electrochemical measurements were performed using a three-electrode cell system connected to a potentiostat (Autolab PGSTAT302N, Metrohm). The HER activity of the prepared samples was measured using LSV in the potential range of $-0.2\ V_{SCE}$~$-0.8\ V_{SCE}$ at a scan rate of 10 mV/s, with a carbon rod and SCE used as the counter and reference electrodes, respectively. To analyze the electrochemical surface area (ECSA), repeated CV was conducted in the non-faradaic potential range with varying scan rates of 25, 50, and 75 mV/s in 0.5 M H_2SO_4. All of the solutions used for the electrochemical measurements were purged with N_2 gas for 30 min prior to the experiment. All of the measured potentials were converted to RHE potentials according to $E_{RHE}=E_{SCE}+0.2412+0.0592*pH$.

6. PEMWE Single Cell Test

To operate a PEMWE single cell test, sandwich-type MEA was fabricated by placing a commercial Nafion membrane (212, Dupont. Co.) between the cathode and anode. The fabricated electrode was directly used as the cathode, whereas the electrodeposited IrO_2/CP

(loading: 0.1 mg cm^{-2}) served as the anode. Referring to the previous literature [8], IrO_2 electrodeposition was conducted on the CP substrate at a constant potential of 0.7 V_{SCE} for 600 s in the deposition bath containing 0.1 M $IrCl_4$ precursor. The active area of the MEA was 1.0 cm^2. Prior to the PEMWE operation, deionized water (temperature: 95 °C) was injected into the anode side at a flow rate of 10 ml/min, while the PEMWE single cell was preheated to 90 °C. After stabilizing for 30 min, the PEMWE single cell was operated by stepping the current density to 0.02, 0.05, 0.10, 0.15, 0.20, 0.25, 0.30, 0.40, 0.50, 0.75, and 1.00 A/cm^2. Each current density was maintained for 1 min.

For overpotential analysis, the ohmic resistance (R_{ohm}) of the single cell was measured at a current density of 0.5 A/cm^2 by electrochemical impedance spectroscopy (EIS, Autolab FRA32M, Metrohm) in a frequency range of 10^6 Hz to 10^{-1} Hz. The ohmic overpotential ($\eta_{ohm}=iR_{ohm}$) was calculated, and the kinetic overpotential (η_{kin}) was derived from the Tafel slope. The mass transfer overpotential (η_{mass}) was determined by the remaining overpotential according to $\eta_{mass}=E-E_0-\eta_{kin}-\eta_{ohm}$, where E_0 is the theoretical potential for water electrolysis at 90 °C.

RESULTS AND DISCUSSION

As a metallic support, the CF was prepared on the pretreated CP substrate (Fig. 1(a)) using a two-step electrodeposition method. The first step was galvanostatic electrodeposition performed at a low current of −13.3 mA/cm^2 for 60 s for the formation of Cu seeds on the CP surface. As shown in Fig. 1(b), a number of Cu particles were observed with high coverage. In the second step, the galvanostatic electrodeposition was conducted at a high current of −885.0 mA/cm^2 for 60 s to facilitate simultaneous Cu^{2+} and H^+ reduction. The vigorous H_2 generation facilitated the formation of 3-D networked CF with a pore size of ~30 μm (Fig. 1(c)). In the high-magnification FESEM image (inset of Fig. 1(c)), highly-roughened Cu dendrites were observed, potentially indicating that the CF can provide a large number of active sites for electrocatalyst formation as well as facilitate the enhanced charge transport for the catalyst surface-electrolyte interfaces in order to improve the HER performance [32]. Subsequently, Ni-P was electrodeposited on CF/CP. As shown in Fig. 1(d), spherical Ni-P particles were observed with high coverage on the surface of CF/CP while the overall porous structure of CF was maintained. The positive LSV scan of Ni-P/CF/CP without a Cu oxidation peak obtained in 0.1 M KOH demonstrated that CF fully covered by Ni-P was obtained (Fig. S1) [46]. In addition, the XRD pattern of Ni-P/CF/CP, which was the same with CF/CP, demonstrated the amorphous structure of Ni-P deposit (Fig. S2).

To investigate the electrochemical properties of the as-prepared Ni-P/CF/CP, LSV was conducted in 0.5 M H_2SO_4 electrolyte (Fig. S3). In the negative scan, an anodic current was observed in the vicinity of 0.0 V_{RHE} that may be due to the electrochemical dissolution of excess Ni metal in the Ni-P/CF/CP formed during the Ni-P electrodeposition [39]. Therefore, an anodic leaching process was performed as the post-treatment for Ni-P/CF/CP because it was reported that an appropriate potential facilitated the selective dissolution of Ni in the electrodeposited Ni-P [42]. Fig. 2(a) shows positive scans of LSV for CF/CP and Ni-P/CF/CP in the 0.5 M H_2SO_4 electrolyte. For the CF/CP, the anodic peak observed at 0.65 V_{RHE} corresponded to the Cu oxidation in the CF/CP catalyst. On the other hand, for NiP/CF/CP, the anodic peak appeared in a

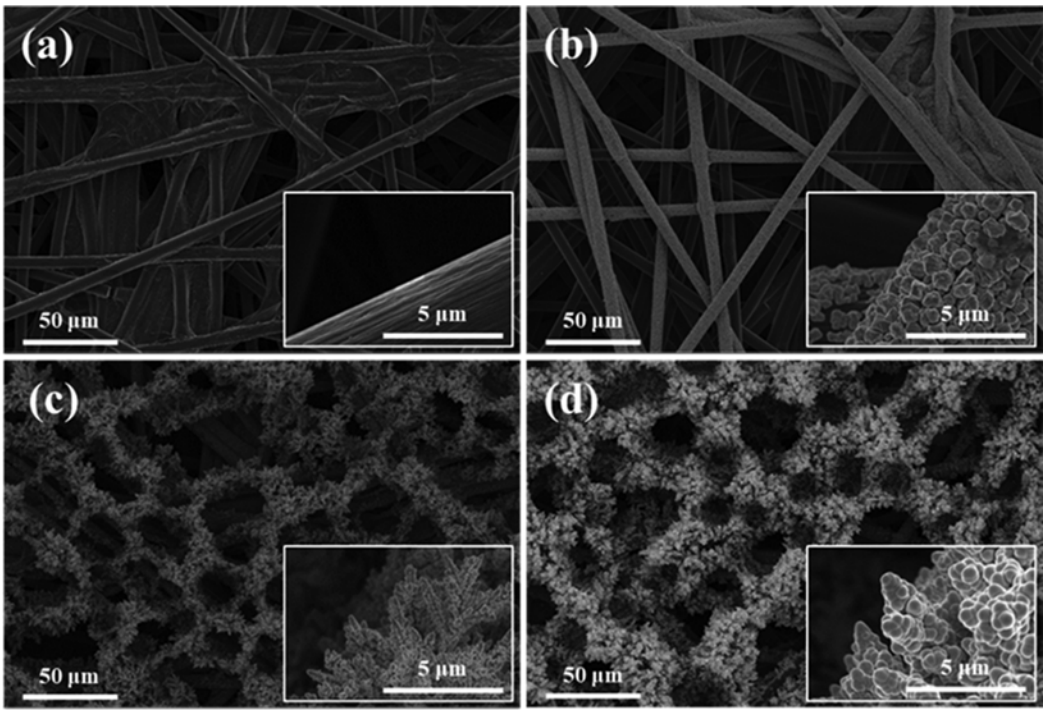

Fig. 1. FESEM images of (a) pretreated CP, (b) after first Cu electrodeposition, (c) after second Cu electrodeposition, and (d) after Ni-P electrodeposition.

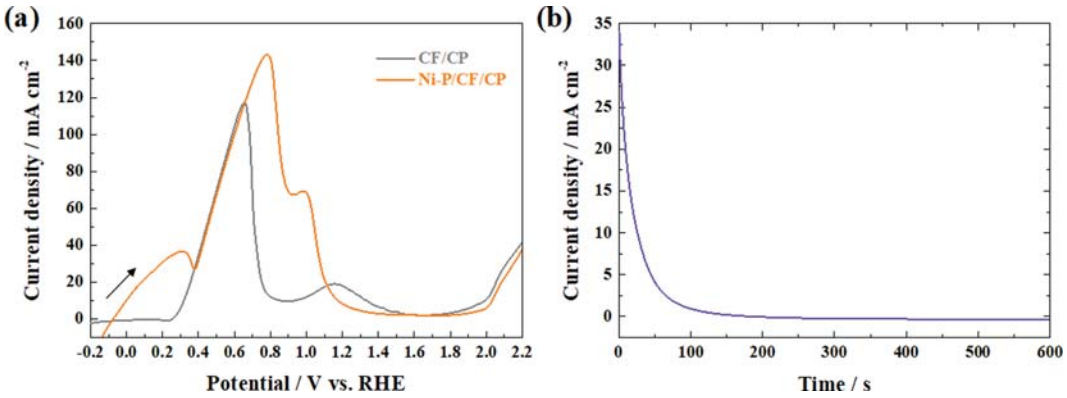

Fig. 2. (a) LSV curves of CF/CP and Ni-P/CF/CP at a scan rate of 10 mV/s in the N_2-purged 0.5 M H_2SO_4 electrolyte (b) Chronoamperometry of NiP/CF/CP for the anodic leaching process at 0.17 V_{RHE} for 600 s.

more negative potential range before the Cu oxidation peak, thus demonstrating the dissolution of excess Ni metal [42]. Further positive sweep showed two anodic peaks representing the oxidation of Cu exposed by Ni dissolution and the oxidation of Ni-P, respectively. Based on the LSV analysis, the anodic leaching process on the Ni-P/CF/CP was conducted at the constant potentials of 0.07, 0.17, and 0.27 V_{RHE} (Fig. S4). Considering the morphology of the samples after these processes, the anodic leaching potential was chosen as 0.17 V_{RHE}, and the results of chronoamperometry measurements carried out for 600 s are shown in Fig. 2(b). The anodic current density decreased rapidly at the initial stage and then mostly saturated at 0 after 300 s, indicating the completion of Ni dissolution.

The anodic leaching process was performed at a constant potential of 0.17 V_{RHE} for various leaching times, and the obtained samples were named L#Ni-P/CF/CP (#: anodic leaching time in s). As shown in Fig. 3, as the anodic leaching time increased, the size of the spherical Ni-P particles gradually decreased while the overall porous structure was maintained. Fig. 4(a) demonstrates the positive scan of the LSV curves for the as-deposited Ni-P/CF/CP and the L#Ni-P/CF/CP performed in the N_2-purged 0.5 M H_2SO_4 electrolyte. With the increase in the anodic leaching time, the first peak current demonstrating the Ni dissolution gradually decreased, indicating that the amount of the remaining Ni metal at the surface of the L#NiP/CF/CP decreased continuously. Then, at the leaching time of 300 s, the Ni metal was completely eliminated as indicated by the absence of the anodic current. Meanwhile, the two anodic peaks observed at more positive potential ranges were similar for all of the samples. Fig. 4(b) shows the current density recorded at 0.17 V_{RHE} in the LSV curves and the atomic Ni bulk composition of the as-deposited Ni-P/CF/CP and the L#Ni-P/CF/CP. The atomic Ni bulk composition first gradually decreased from 89.6% to 75.6% as the anodic leaching time increased from 0 to 300 s, and then became saturated, corresponding to the decrease in the current density at 0.17 V_{RHE}.

Fig. 5(a) and 5(b) show the XPS spectra of the as-prepared Ni-P/CF/CP and L#Ni-P/CF/CP. For Ni-P/CF/CP, its Ni 2p XPS spectrum was deconvoluted into four peaks at 852.4, 852.9, 856.3, and 860.3 eV. The Ni $2p_{3/2}$ peak binding energies of 852.4 eV and 852.9 eV represent metallic Ni and the oxidized $Ni^{\delta+}$ state, respectively [47]. In addition, the peak at 856.3 eV reflected the formation of Ni native oxide [47]. As the anodic leaching time increased, the peak binding energy of metallic Ni shifted to higher energy due to

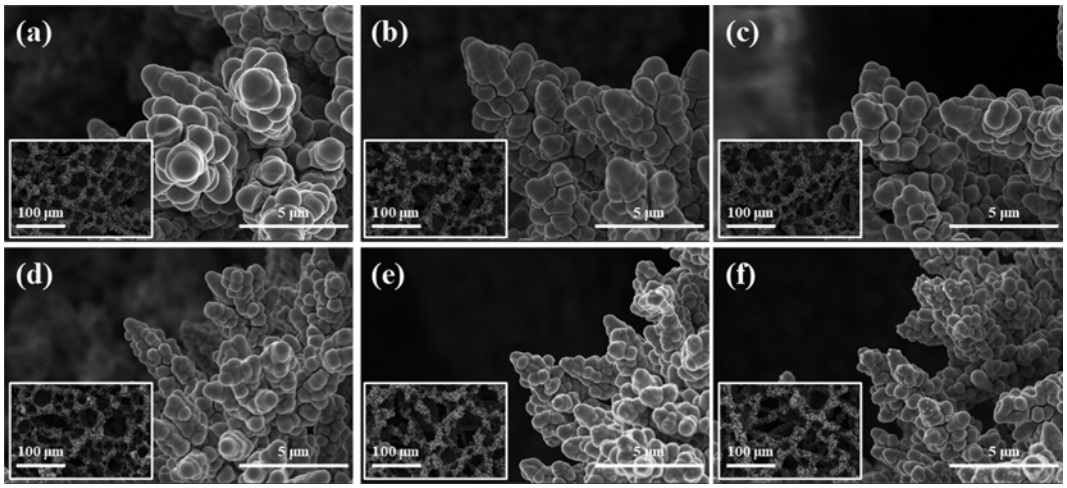

Fig. 3. FESEM images of Ni-P/CF/CP after the anodic leaching process at 0.17 V_{RHE} in N_2-purged 0.5 M H_2SO_4 for durations of: (a) 20 s, (b) 50 s, (c) 70 s, (d) 100 s, (e) 300 s, and (f) 600 s.

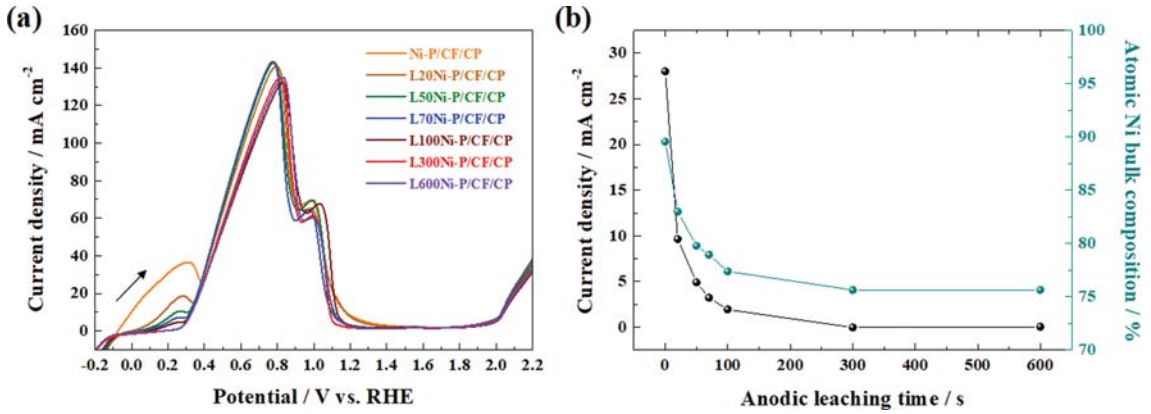

Fig. 4. (a) LSV curves of Ni-P/CF/CP and L#/NiP/CF/CP at a scan rate of 10 mV/s in the N_2-purged 0.5 M H_2SO_4 electrolyte. (b) Current density recorded at 0.17 V_{RHE} from the LSV curves in Fig. 4(a) and atomic Ni bulk composition measured by EDS as a function of the anodic leaching time.

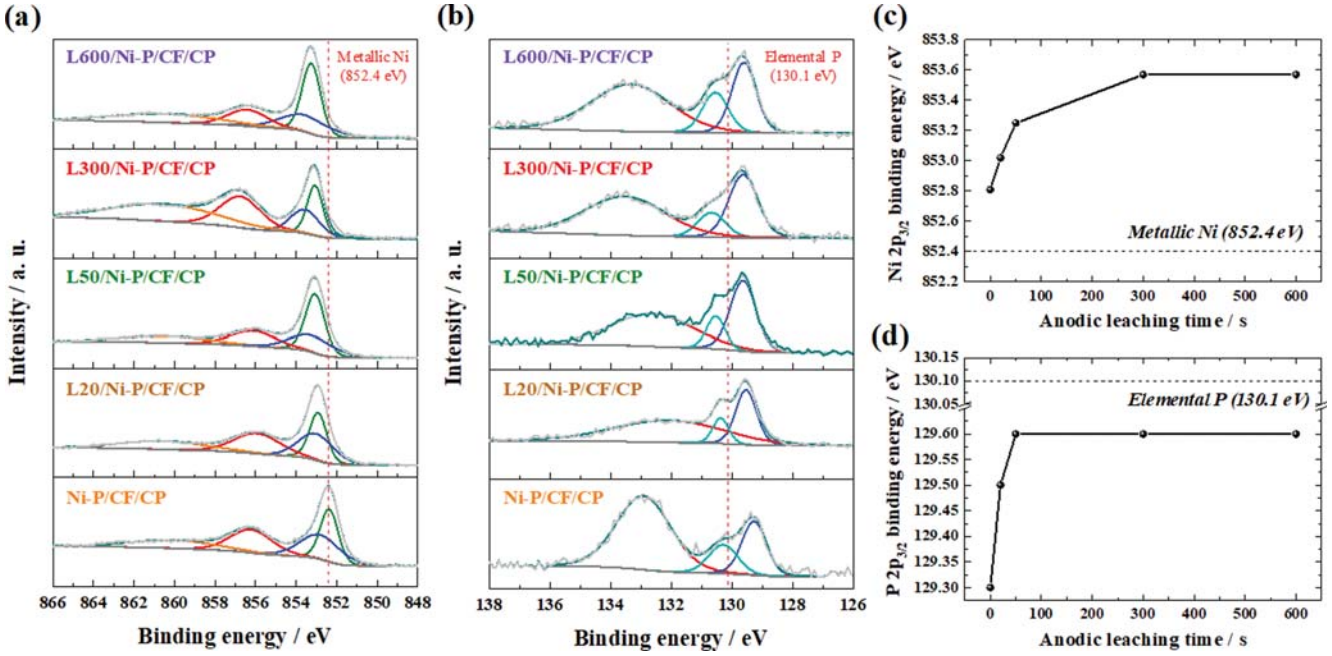

Fig. 5. XPS spectra of the NiP/CF/CP and L#/NiP/CF/CP catalysts after various anodic leaching times: (a) Ni 2p and (b) P 2p regions. Binding energies of (c) Ni $2p_{3/2}$ and (d) P $2p_{3/2}$ plotted as a function of the anodic leaching time.

the decrease in the Ni/P ratio at the surface of L#Ni-P/CF/CP after the anodic leaching process. This indicates electron transfer from Ni to P due to their different electronegativity. Supporting this conclusion, the P 2p spectra correspond to reduced electronic structure. Compared to that of elemental P, the P $2p_{3/2}$ peak binding energy of the as-prepared NiP/CF/CP and L#/NiP/CF/CP showed a binding energy shift to lower energies [48]. As the anodic leaching time increased, the P $2p_{3/2}$ peak gradually shifted toward the binding energy of elemental P due to the decrease in the Ni/P ratio at the surface. The $2p_{3/2}$ peak binding energy for Ni and P is summarized in Fig. 5(c) and 5(d), respectively. The binding energies were saturated after the anodic leaching time of 300 s, indicating that selective Ni dissolution was completed without Ni-P oxidation at the anodic leaching potential.

The HER activities of CF/CP and L#Ni-P/CF/CP were measured by LSV in the N_2-purged 0.5 M H_2SO_4 electrolyte, and the obtained LSV curves with the iR correction applied are shown in Fig. 6(a). The CF/CP sample showed negligible current density in the potential range. Compared to the LSV curve of the as-prepared Ni-P/CF/CP (Fig. S3), all L#Ni-P/CF/CP samples demonstrated the absence of the anodic current density in the vicinity of 0 V_{RHE}, indicating the decreased surface proportion of the Ni metal in the L#Ni-P/CF/CP after the anodic leaching process. The L20Ni-P/CF/CP and L50Ni-P/CF/CP samples exhibited similar HER performance, higher than those of the L300Ni-P/CF/CP and L600Ni-P/CF/CP samples. Fig. 6(b) shows the Tafel plots of the LSV curves for L#Ni-P/CF/CP. The Tafel slopes for all L#Ni-P/CF/CP samples were in the range of 66-84 mV/dec, demonstrating that HER fol-

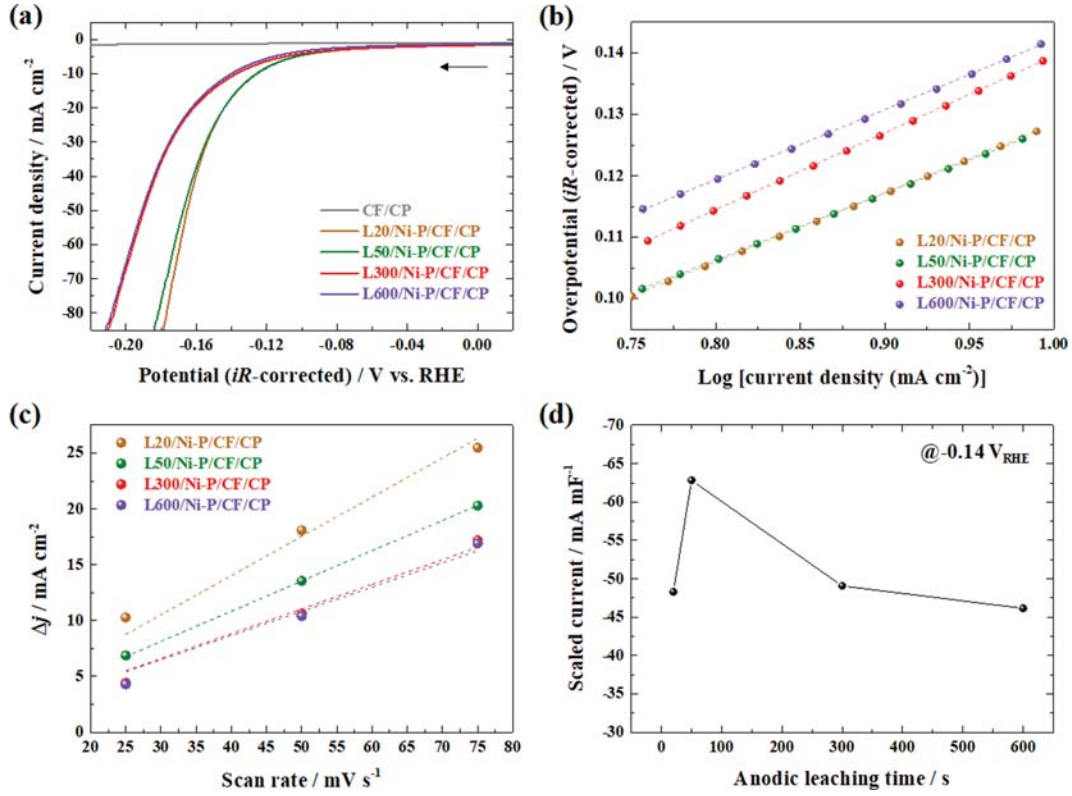

Fig. 6. (a) LSV curves of L#Ni-P/CF/CP at a scan rate of 10 mV/s in the N_2-purged 0.5 M H_2SO_4 electrolyte. (b) Tafel plots for the curves shown in (a). (c) Double layer capacitance measurements for L#/Ni-P/CF/CP. (d) Scaled current recorded at −0.14 V_{RHE} as a function of the anodic leaching time for L#Ni-P/CF/CP.

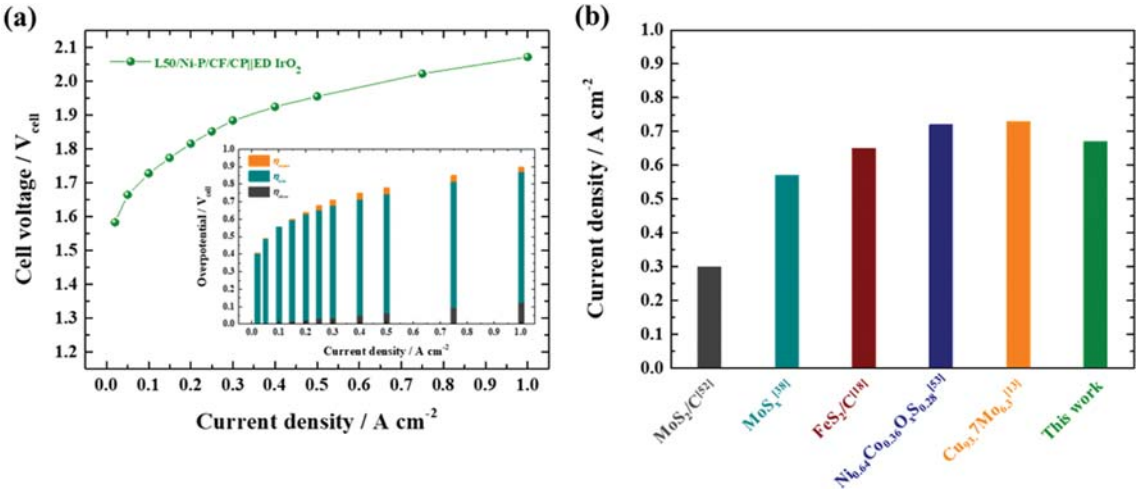

Fig. 7. (a) Polarization curve of a PEMWE single cell with the L50Ni-P/CF/CP cathode and IrO_2 anode. Inset: overpotential analysis for various current densities. (b) PEMWE single cell performance comparison: current densities at 2.0 V_{cell}.

lowed the Volmer-Heyrovsky reaction mechanism [49]. To estimate the ECSA, CV measurements at varying scan rates were conducted for the L#Ni-P/CF/CP samples in the non-faradaic potential range (Fig. S5), and then their double layer capacitances (C_{dl}) were measured with the results shown in Fig. 6(c). It is observed that with increasing anodic leaching time, the slope decreased, indicating the decrease in the ECSA. Fig. 6(d) demonstrates the scaled current representing the intrinsic HER activity of L#Ni-P/CF/CP as a function of the anodic leaching time. The maximum intrinsic HER activity was obtained for the L50Ni-P/CF/CP samples; this may be related to the modified electronic structure of this sample that affects the ΔG_H^* on the surface of L#Ni-P/CF/CP.

Based on the results described above, L50Ni-P/CF/CP was chosen as the cathode for the PEMWE single cell operation. Fig. 7(a)

shows the I-V curve of the PEMWE single cell based on L50Ni-P/CF/CP. The Nyquist plot obtained by EIS measurements shows a low ohmic resistance of the 127 mΩ·cm^2, revealing the good electrical conductivity and small contact resistance at the catalyst-membrane interface (Fig. S6) [50,51]. The overpotential of the single cell was divided into three contributions of η_{ohm}, η_{kin}, and η_{mass} (inset of Fig. 7(a)). The η_{kin} contribution was dominant due to the limited performance of the non-noble cathode. On the other hand, the low ohmic resistance facilitated the small η_{ohm} contribution. Both of these contributions gradually increased with increasing current density. Meanwhile, η_{mass} also accounted for a small fraction of the total overpotential, particularly in the high current density region where the gas evolutions were severely carried out. The porous structure of the L50Ni-P/CF/CP cathode enabled enhanced mass transport compared to the conventional cathode prepared by the spray coating method [18,52]. At a cell voltage of 2.0 V, the current density was measured as 0.67 A/cm^2, higher or comparable to that obtained using the state-of-the-art non-noble metal-based cathodes reported in recent literature [13,18,38,52,53].

CONCLUSION

We have demonstrated a simple fabrication method for Ni-P-based cathodes using electrochemical methods. As a metallic substrate, the porous CF on CP provided a large number of active sites for Ni-P electrodeposition and fast charge transfer at the catalyst/electrolyte interfaces. By varying the anodic leaching time, it was revealed that the electronic structure of L#/Ni-P/CF/CP was changed by the gradual removal of the excess Ni metal in Ni-P, affecting its intrinsic HER activity. The optimized sample (L50Ni-P/CF/CP) was used as the cathode for the PEMWE single cell, and the analysis of the overpotential results demonstrated the low η_{ohm} and η_{mass} related to the low ohmic resistance and enhanced mass transfer arising from the appropriate structure of the cathode. The PEMWE single cell exhibited a current density of 0.67 A/cm^2 at 2.0 V_{cell} that was higher than, or comparable to, those obtained for other non-noble metal-based cathodes reported in previous studies.

ACKNOWLEDGEMENTS

This research was supported by the National Research Foundation of Korea (NRF) grant funded by the Korean government MSIT (2019M3E6A1103818) and by the Chung-Ang University Research Scholarship Grant in 2019.

SUPPORTING INFORMATION

Additional information as noted in the text. This information is available via the Internet at http://www.springer.com/chemistry/journal/11814.

REFERENCES

1. J. A. Turner, *Science*, **305**, 972 (2004).
2. O. Khadelev and J. A. Turner, *Science*, **280**, 425 (1998).
3. M. Wang, Z. Wang, X. Gong and Z. Guo, *Renew. Sust. Energy Rev.*, **29**, 573 (2014).
4. S. E. Hosseini and M. A. Wahid, *Renew. Sust. Energy Rev.*, **57**, 850 (2016).
5. M. Carmo, D. L. Fritz, J. Mergel and D. Stolten, *Int. J. Hydrogen Energy*, **38**, 4901 (2013).
6. C. C. Pavel, F. Cecconi, C. Emiliani, S. Santiccioli, A. Scaffidi, S. Catanorchi and M. Comotti, *Angew. Chem. Int. Ed.*, **53**, 1378 (2014).
7. X. Zou and Y. Zhang, *Chem. Soc. Rev.*, **44**, 5148 (2015).
8. B.-S. Lee, S. H. Ahn, H.-Y. Park, I. Choi, S. J. Yoo, H.-J. Kim, D. Henkensmeier, J. Y. Kim, S. Park, S. W. Nam, K.-Y. Lee and J. H. Jang, *Appl. Catal. B-Environ.*, **179**, 285 (2015).
9. J. D. Holladay, J. Hu, D. L. King and Y. Wang, *Catal. Today*, **139**, 244 (2009).
10. H. Yu, L. Bonville, J. Jankovic and R. Maric, *Appl. Catal. B-Environ.*, **260**, 118194 (2020).
11. K. Ojha, S. Saha, P. Dagar and A. K. Ganguli, *Phys. Chem. Chem. Phys.*, **20**, 6777 (2018).
12. J. H. Kim, J. Kim, H. Kim, J. Kim and S. H. Ahn, *J. Ind. Eng. Chem.*, **79**, 255 (2019).
13. H. Kim, E. Hwang, H. Park, B.-S. Lee, J. H. Jang, H.-J. Kim, S. H. Ahn and S.-K. Kim, *Appl. Catal. B-Environ.*, **206**, 608 (2017).
14. J. Chen, Y. Yang, J. Su, P. Jiang, G. Xia and Q. Chen, *ACS Appl. Mater. Interfaces*, **9**, 3596 (2017).
15. J. Masa, S. Barwe, C. Andronescu, I. Sinev, A. Ruff, K. Jayaramulu, K. Elumeeva, B. Konkena, B. R. Cuenya and W. Schuhmann, *ACS Energy Lett.*, **1**, 1192 (2016).
16. X. Wang, Y. V. Kolen'ko, X.-Q. Bao, K. Kovnir and L. Liu, *Angew. Chem. Int. Ed.*, **54**, 8188 (2015).
17. P. Cao, J. Peng, J. Li and M. Zhai, *J. Power Sources*, **347**, 210 (2017).
18. C. D. Giovanni, Á. Reyes-Carmona, A. Coursier, S. Nowak, J. M. Grenèche, H. Lecoq, L. Mouton, J. Rozière, D. Jones, J. Peron, M. Giraud and C. Tard, *ACS Catal.*, **6**, 2626 (2016).
19. S. Gupta, N. Patel, A. Miotello and D. C. Kothari, *J. Power Sources*, **279**, 620 (2015).
20. X. Xu, Y. Deng, M. Gu, B. Sun, Z. Liang, Y. Xue, Y. Guo, J. Tian and H. Cui, *Appl. Surf. Sci.*, **470**, 591 (2019).
21. W.-F. Chen, K. Sasaki, C. Ma, A. I. Frenkel, N. Marinkovic, J. T. Muckerman, Y. Zhu and R. R. Adzic, *Angew. Chem. Int. Ed.*, **51**, 6131 (2012).
22. J. Xie, S. Li, X. Zhang, J. Zhang, R. Wang, H. Zhang, B. Pan and Y. Xie, *Chem. Sci.*, **5**, 4615 (2014).
23. J. Kibsgaard, C. Tsai, K. Chan, J. D. Benck, J. K. Nørskov, F. Abild-Pedersen and T. F. Jaramillo, *Energy Environ. Sci.*, **8**, 3022 (2015).
24. F. Wang, T. A. Shifa, X. Zhan, Y. Huang, K. Liu, Z. Cheng, C. Jiang and J. He, *Nanoscale*, **7**, 19764 (2015).
25. E. J. Popczun, J. R. McKone, C. G. Read, A. J. Biacchi, A. M. Wiltrout, N. S. Lewis and R. E. Schaak, *J. Am. Chem. Soc.*, **135**, 9267 (2013).
26. Y. Pan, Y. Liu, J. Zhao, K. Yang, J. Liang, D. Liu, W. Hu, D. Liu, Y. Liu and C. Liu, *J. Mater. Chem. A*, **3**, 1656 (2015).
27. Y.-H. Chung, K. Gupta, J.-H. Jang, H. S. Park, I. Jang, J. H. Jang, Y.-K. Lee, S.-C. Lee and S. J. Yoo, *Nano Energy*, **26**, 496 (2016).
28. Y. Li and C. Zhao, *Chem. Mater.*, **28**, 5659 (2016).
29. X. Wang, R. Tong, Y. Wang, H. Tao, Z. Zhang and H. Wang, *ACS Appl. Mater. Interfaces*, **8**, 34270 (2016).
30. J. Kim, H. Kim, J. Kim, J. H. Kim and S. H. Ahn, *J. Alloy Compd.*,

807, 148813 (2019).
31. X. Ma, Y. Chang, Z. Zhang and J. Tang, *J. Mater. Chem. A*, **6**, 2100 (2018).
32. C. Zhang, Y. Xie, H. Deng, C. Zhang, J.-W. Su, Y. Dong and J. Lin, *Int. J. Hydrogen Energy*, **43**, 7299 (2018).
33. X. Yang, A.-Y. Lu, Y. Zhu, M. N. Hedhili, S. Min, K.-W. Huang, Y. Han and L.-J. Li, *Nano Energy*, **15**, 634 (2015).
34. Y. Pan, Y. Liu and C. Liu, *J. Power Sources*, **285**, 169 (2015).
35. Y. Pan, Y. Lin, Y. Chen, Y. Liu and C. Liu, *J. Mater. Chem. A*, **4**, 4745 (2016).
36. S. Siracusano, N. V. Dijk, E. Payne-Johnson, V. Baglio and A. S. Aricò, *Appl. Catal. B-Environ.*, **164**, 488 (2015).
37. H. Kim, S. Choe, H. Park, J. H. Jang, S. H. Ahn and S.-K. Kim, *Nanoscale*, **9**, 19045 (2017).
38. J. H. Kim, H. Kim, J. Kim, H. J. Lee, J. H. Jang and S. H. Ahn, *J. Power Sources*, **392**, 69 (2018).
39. M. Ledendecker, J. S. Mondschein, O. Kasian, S. Geiger, D. Göhl, M. Schalenbach, A. Zeradjanin, S. Cherevko, R. E. Schaak and K. Mayrhofer, *Angew. Chem. Int. Ed.*, **56**, 9767 (2017).
40. A. R. J. Kucernak and V. N. N. Sundaram, *J. Mater. Chem. A*, **2**, 17435 (2014).
41. Y. Tan, H. Wang, P. Liu, Y. Shen, C. Cheng, A. Hirata, T. Fujita, Z. Tang and M. Chen, *Energy Environ. Sci.*, **9**, 2257 (2016).
42. J. Kim, J. Kim, H. Kim and S. H. Ahn, *ACS Appl. Mater. Interfaces*, **11**, 30774 (2019).
43. J.-D. Lin and C.-T. Chou, *Surf. Coat.*, **325**, 360 (2017).
44. V. Vosoughi, S. Badoga, A. K. Dalai and N. Abatzoglou, *Ind. Eng. Chem. Res.*, **55**, 6049 (2016).
45. D. Nam, R. Kim, D. Han, J. Kim and H. Kwon, *Electrochim. Acta*, **56**, 9397 (2011).
46. J. C. Hamilton, J. C. Farmer and R. J. Anderson, *J. Electrochem. Soc.*, **133**, 739 (1986).
47. L. Yan, P. Dai, Y. Wang, X. Gu, L. Li, L. Cao and X. Zhao, *ACS Appl. Mater. Interfaces*, **9**, 11642 (2017).
48. Z. Zhou, L. Wei, Y. Wang, H. E. Karahan, Z. Chen, Y. Lei, X. Chen, S. Zhai, X. Liao and Y. Chen, *J. Mater. Chem. A*, **5**, 20390 (2017).
49. C. G. Morales-Guio, L.-A. Stern and X. Hu, *Chem. Soc. Rev.*, **43**, 6555 (2014).
50. J. Mo, Z. Kang, S. T. Retterer, D. A. Cullen, T. J. Toops, J. B. Green, M. M. Mench and F.-Y. Zhang, *Sci. Adv.*, **2**, 1600690 (2016).
51. Z. Kang, G. Yang, J. Mo, Y. Li, S. Yu, D. A. Cullen, S. T. Retterer, T. J. Toops, G. Bender, B. S. Pivovar, J. B. Green and F.-Y. Zhang, *Nano Energy*, **47**, 434 (2018).
52. T. Corrales-Sánchez, J. Ampurdanés and A. Urakawa, *Int. J. Hydrogen Energy*, **39**, 20837 (2014).
53. H. Kim, J. Kim, S.-K. Kim and S. H. Ahn, *Appl. Catal. B-Environ.*, **232**, 93 (2018).

Supporting Information

Electrodeposited nickel phosphide supported by copper foam for proton exchange membrane water electrolyzer

Kyurim Yeon[‡], Junhyeong Kim[‡], Hyunki Kim, Wenwu Guo, Gyeong Ho Han, Seokjin Hong, and Sang Hyun Ahn[†]

School of Chemical Engineering and Material Science, Chung-Ang University,
84 Heukseokno, Dongjak-gu, Seoul 06974, Korea
(*Received 24 March 2020 • Revised 6 May 2020 • Accepted 20 May 2020*)

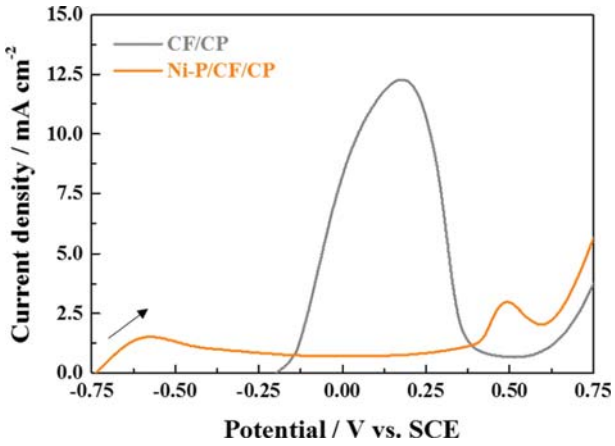

Fig. S1. LSV curves of CF/CP and Ni-P/CF/CP at a scan rate of 10 mV/s in the N_2-purged 0.1 M KOH electrolyte.

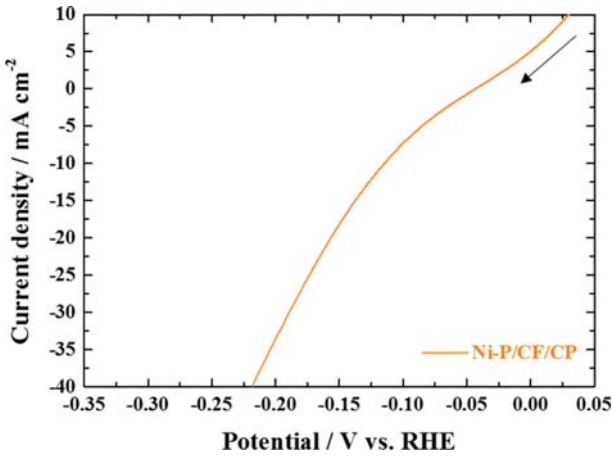

Fig. S3. LSV curve of Ni-P/CF/CP at a scan rate of 10 mV/s in the N_2-purged 0.5 M H_2SO_4 electrolyte.

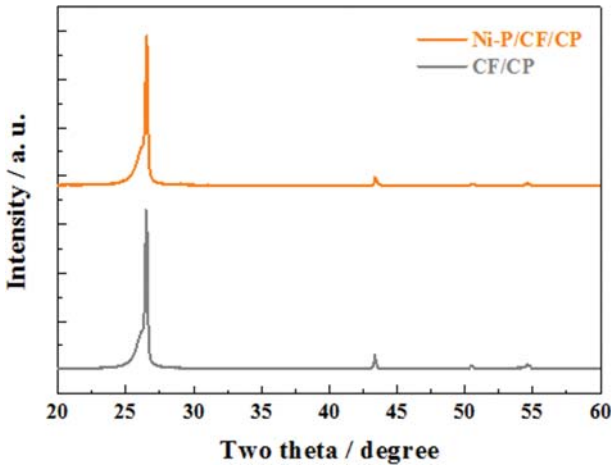

Fig. S2. XRD patterns of CF/CP and Ni-P/CF/CP.

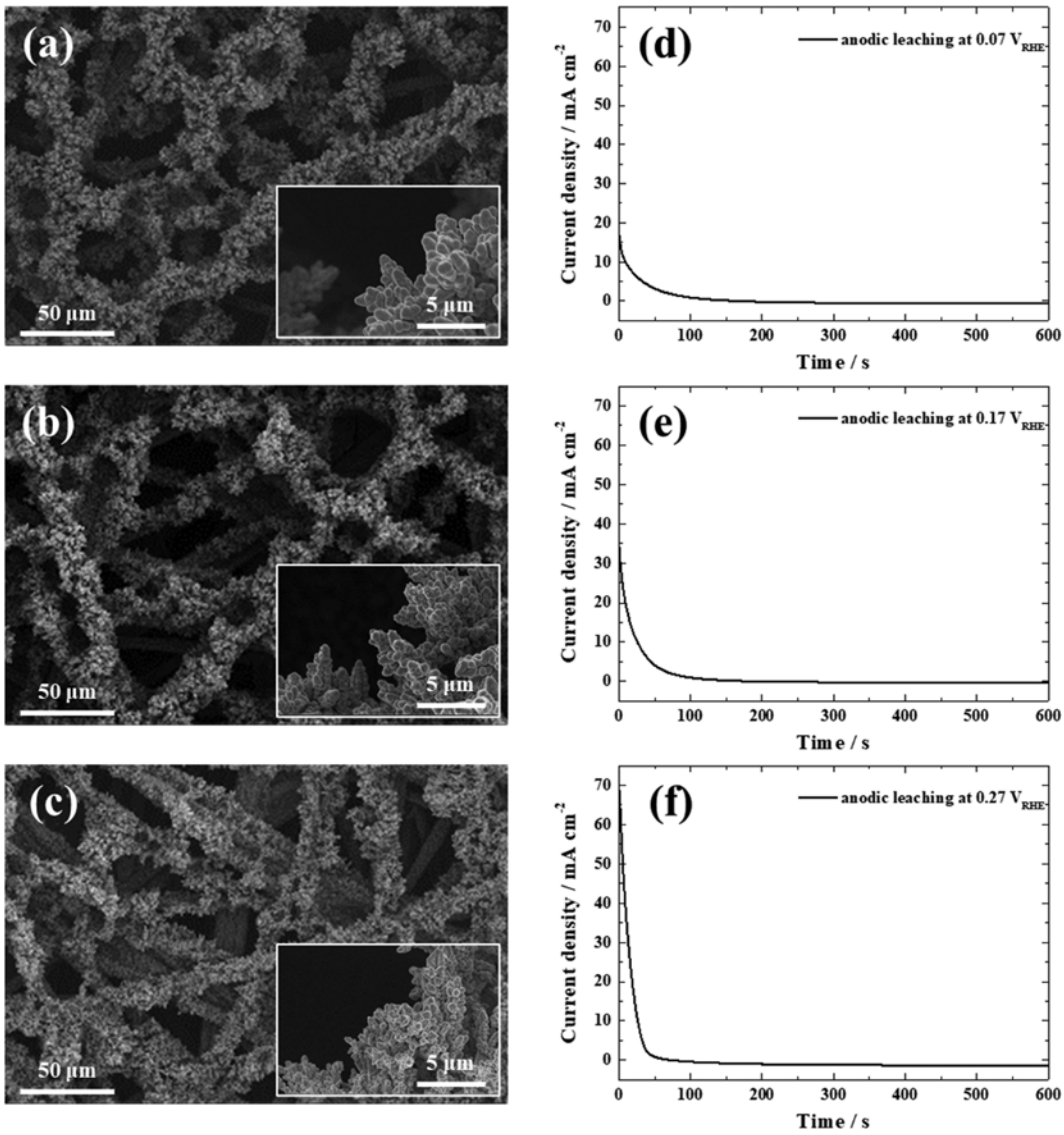

Fig. S4. FESEM images of Ni-P/CF/CP after anodic leaching for 600 s at various potentials: (a) 0.07 V_{RHE}, (b) 0.17 V_{RHE}, and (c) 0.27 V_{RHE}. Chronoamperometry of the anodic leaching process for 600 s at various potentials: (d) 0.07 V_{RHE}, (e) 0.17 V_{RHE}, and (f) 0.27 V_{RHE}.

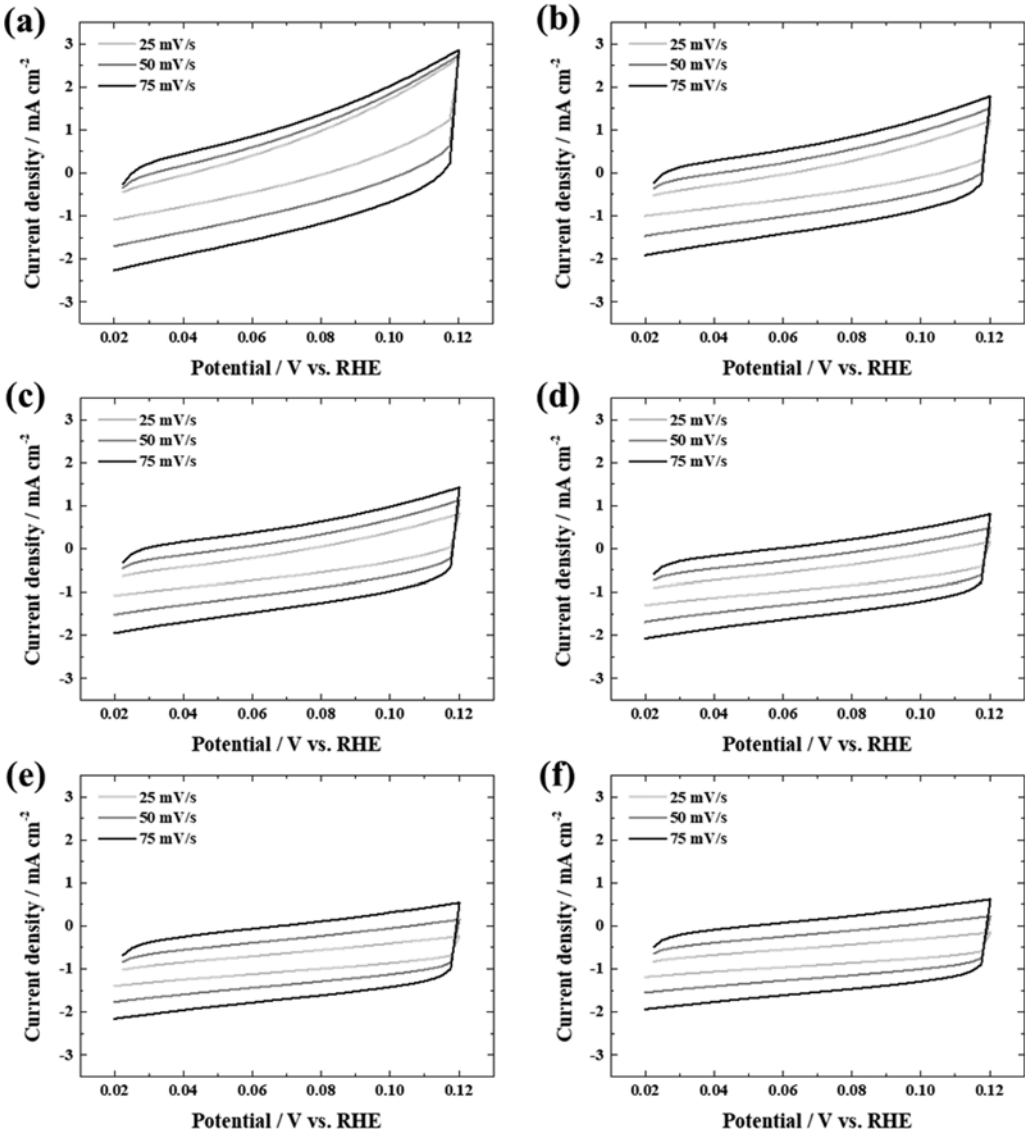

Fig. S5. Cyclic voltammetry curves in the N_2-purged 0.5 M H_2SO_4 electrolyte obtained at different scan rates: (a) L20Ni-P/CF/CP, (b) L50Ni-P/CF/CP, (c) L70Ni-P/CF/CP, (d) L100Ni-P/CF/CP, (e) L300Ni-P/CF/CP, and (f) L600Ni-P/CF/CP.

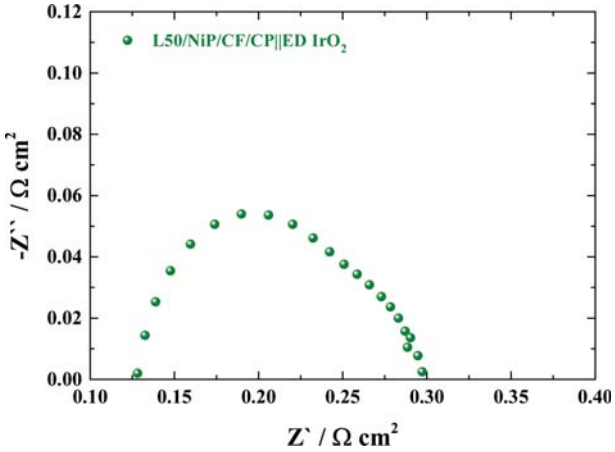

Fig. S6. EIS analysis of PEMWE single cell with L50/NiP/CF/CP and an IrO_2 anode recorded at 0.5 A cm^{-2}.